Materials Today Communications 38 (2024) 107889

Contents lists available at ScienceDirect

Materials Today Communications

journal homepage: www.elsevier.com/locate/mtcomm

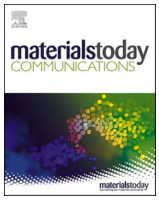

Material extrusion of metals: Enabling multi-material alloys in additive manufacturing

Karim Asami [a,*], José M. Crego Lozares [a,b], Abid Ullah [a,b,*], Bastian Bossen [a], Leighton Clague [c], Claus Emmelmann [a]

[a] Institute of Laser and System Technologies, Hamburg University of Technology, Harburger Schloßstraße 28, Hamburg 21079, Germany
[b] Centre for Additive Manufacturing, School of Engineering, RMIT University, Melbourne, VIC 3000, Australia
[c] XERION Berlin Laboratories GmbH, Groß-Berliner Damm 84A, Berlin 12487, Germany

ARTICLE INFO

Keywords:
Additive Manufacturing
Multi-Material Alloys
MEX/M Technology
316 L
17–4PH
Sintering
Filament Feedstock

ABSTRACT

This article discusses the use of Material Extrusion of Metals (MEX/M - defined in ISO/ASTM 52900) technology for producing multi-material components, which offers a cost-effective and efficient method without requiring major adaptations to existing equipment. The article presents the successful manufacture of 316L/17–4PH multi-alloy steel cubes for four different sintering temperatures using commercially available equipment and feedstock. The feasibility study of the multi-material samples was supported by analyzing the shrinkage, optical density, and microstructure as output parameters. Unlike other works, the multi-material produced parts showed regular shrinkage behaviour and no major deformation, indicating the possibility of creating functional parts without the need for post-processing. Interestingly, relevant findings were made on the different shrinkage values obtained for the constellations considered. Further in-depth investigation of each parameter involved in all the stages of the chain value (extrusion, debinding, and sintering) will be key to support the present results. Additional research into the mechanical and magnetic properties of the samples produced could lead this combination of materials to applications in various industries including automotive and aerospace.

1. Introduction

The advent of additive manufacturing (AM) has furthered many areas of industry with the ability to create novel geometries that were not possible with long-established manufacturing processes, such as milling and casting [1,2]. By far the most widespread AM process is the Material Extrusion of Polymers (MEX/P), due to its low cost and fast production of parts [3,4]. A recent development within the AM space is the filament-based material extrusion of metals (MEX/M - defined in ISO/ASTM 52900), also known as Metal Fused-Filament Fabrication (FFF) as per ISO 52900, whereby a metallic powder held within a polymer matrix is extruded using MEX/P style printers [5,6]. Similar to Metal Injection Molding (MIM), the part is then debound chemically and/or thermally [7,8], and then placed in a sintering furnace until it densifies. The result is a high-density metallic part with densities in the range of 95–98% [9]. Due to its similarity to both MEX/P and MIM, MEX/M has a solid foundation in the literature [10–13]. Thus, a wide range of materials is readily available in different forms (rods, pellets, cartridges) due to the usage of feedstock similar to that used in MIM [14,15].

One interesting use case of MIM is Multi-material (MM) parts. Previously referred to as two-component MIM (2 C-MIM) different materials are formed together during injection molding and are subsequently debound and co-sintered [16]. This allows not only for a reduction in the amount of post-processing required but also increases the functionality of parts [17]. A range of different material combinations have already been tested, such as steel-steel [18,19], other metal-metal [20–22] metal-ceramic [17,23] as well as ceramic-ceramic [24,25]. Previous MM studies using 2 C-MIM have generally necessitated the use of adjusted powder composition fraction to yield successful results [17,19]. Parallel to MEX/M, there is also existing research regarding MM parts produced using MEX/P, where the discrete deposition of multiple materials using separate nozzles, as well as the mixing of two materials within a single nozzle head has also been investigated [26,27]. Late investigations have also focused on optimizing the interlayer strength of the polymer parts, especially at the interface between two materials [28–31]. Since the

* Corresponding authors at: Institute of Laser and System Technologies, Hamburg University of Technology, Harburger Schloßstraße 28, Hamburg 21079, Germany.
E-mail addresses: karim.asami@tuhh.de (K. Asami), abid.ullah@tuhh.de (A. Ullah).

https://doi.org/10.1016/j.mtcomm.2023.107889
Received 10 September 2023; Received in revised form 12 December 2023; Accepted 15 December 2023
Available online 19 December 2023

MEX/P and MEX/M share the same hardware, the previous study could be covered for metal MM parts.

MM deposition using MEX/M is therefore well-posed, due to the fact that equipment and research exist on the MEX/P side, while the feedstock material combinations have been investigated from the MIM side. Conversely, MEX/M offers some advantages with respect to MEX/P and MIM. Namely, the feedstock of different MEX/M materials has a similar, or custom, polymer matrix. This allows for uniform printing parameters during the printing stage, which leads to better adhesion between different layers. With respect to MIM, MEX/M can create parts that aren't fully dense, i.e. parts with an infill pattern as typically seen in MEX/P, which can help speed the debinding process [32]. Additionally, the geometric freedom enabled by MEX/M that is not accessible through MIM could be used to fine-tune the interface of two materials, to increase the chances of successful sintering.

To date, there has been a very limited amount of research regarding MM parts produced using MEX/M. Mousapour et al. [33] investigated the use of 316L stainless steel and high-carbon iron MM cubes. Mixed, coupled, and functionally graded samples were produced, using commercially available filament with mixed results. By optimizing the sintering conditions concerning temperature, holding time, and heating rate, densities of 91–92% were achieved. All samples showed extensive deformation, indicating the need for post-processing to obtain usable components. Abel et al. [34] experimented with Zirconia/17–4PH stainless steel components, with self-prepared feedstock. Samples were produced without major defects, showing good adhesion at the interface on a macroscopic level. To that end, existing literature lacks a thorough investigation of manufacturing MM components using MEX/M, despite the literature that exists from MIM already, as well as MEX/M being well suited to MMAM concerning other AM processes, especially in terms of cost-effectiveness [35].

Depending on the material combination, there is a wide range of applications for MM MEX/M components. The work of Imgrund et al. [19] details the manufacture of magnetic-nonmagnetic parts using a combination of 17–4PH and 316L stainless steel, albeit with micrometal injection molding. Two demonstrators were produced, one being a magnetic positioning encoder incorporated with a hall sensor, the other being a miniature tachometer. Zirconia/17–4PH components, as produced by Abel et al. [34] can be used to create heating elements, with the electrical conducting stainless steel sitting within an isolating zirconia matrix. 17–4PH/316L was identified as an interesting material combination for MM MEX/M, due to existing research from MIM, the availability of feedstock, as well as the similar sintering behaviors of the two materials [19]. In this paper, the feasibility of MM MEX/M is studied. For this, the bonding between the two materials will be assessed by analyzing the shrinkage, optical density, and microstructure for four proposed sintering temperatures. The aim of this research is to prepare the foundations of the process towards achieving a successful manufacturing process that enables quick changes in design and enables a higher degree of complexity than 2 C-MIM for MM parts.

2. Methods and materials

The test samples are manufactured with AISI 316L (EN 1.4404) and AISI 630 / 17–4PH (EN 1.4542) filament provided by the company PT+A (Dresden, Germany) with the starting powder composition illustrated in Table 1. Powder size distribution was described by the provider as "Fine" grade powder size and was guaranteed for the 17–4PH and 316L powder that were used for the filament production. Fig. 1 shows an SEM image of the debonded filament showing the particles of 17–4PH and 316L, with a powder size in the range of 2 μm to 15 μm respectively. The particles for both alloys are predominantly spherical, exhibiting minimal elliptical necks. In comparison to the reference [36] the particle sizes fall within the range of typical MIM feedstock.

For the investigations of multi-alloy steels in two different constellations, cubic samples with dimensions 10 mm in each space direction were produced and are depicted in Fig. 2. The sintering temperatures and deposition sequences for the samples with the labels S1 to S32 are listed in Table 2. Eight cubes were printed with 50 layers of 316L and 50 layers of 17–4PH. The other eight samples were first printed with 50 layers 17–4PH and then with 50 layers 316L. The slicing and printing parameters were chosen using Simplify 3D software (Simplify 3D, Cincinnati, USA).

Table 1
Starting powder composition for PT+A 316-L (1.4404) and 17–4PH (1.4542) filaments.

Material	316L	17-4PH
Cr	16.8	16
Ni	10.1	4.2
Mo	2.2	0.24
Mn	1.38	0.6
Si	0.74	0.6
P	0.02	0.022
S	0.018	0.003
C	0.004	0.027
Fe	bal.	bal.
Cu	-	4.1
N	-	0.08
O	-	0.06

Eight parts of each constellation were printed using the Renkforce RF 2000 3D printer (Conrad Electronic SE, Hirschau, Germany) with two optimized extruders for direct drive and constant filament feeding. One extruder is equipped with 316L and the other with 17–4PH filament for printing with both filaments to achieve optimal layer connection. Both extruders are driven with the same process parameters which are shown in Table 3. Solvent-based chemical debinding with acetone as solvent was applied in a volume ratio of 8 to 1 between sample and solvent for 12 h at 40 °C as recommended by the provider. An average mass loss after the chemical debinding of the green parts was around 5% as expected from the supplier's advice.

All specimens were thermally debound and sintered in an ExSO90 sinter oven (Aim3D GmbH, Rostock, Germany). Two samples for each of the four different sintering cycles were used, which are illustrated in Fig. 3. The maximum temperature of the sinter cycles is 1286 °C, 1310 °C, 1320 °C, and 1330 °C. The selected temperatures were chosen to achieve a density higher than 95% (MIM standard). The utilization of a 45° alternate filling pattern during the green part printing of the specimen results in a notable reduction in anisotropic shrinkage behavior when the sintering temperature is lowered below that of the single material [37]. Simultaneously, it is known from [19] that the sintering temperature around 1300 °C gives the desired austenitic for 316L, nickel martensite and delta ferrite microstructure for 17–4PH. Furthermore, this sintering temperature also exhibited better ferromagnetic properties [19]. 99,9% Argon was used as the sintering atmosphere and the flow rate for the thermal debinding and sintering step was 1 liter per minute. Thermal debinding and sintering were carried out in one process step. Thermal debinding was performed at two holding times at 325 °C and 600 °C. The holding time was 1 h at 325 °C and 3 h at 600 °C. The heating rate for the first holding time amounted to 300 K/h and for the second holding time to 150 K/h. The heating rate to the sintering temperatures was performed at 150 K/h. Subsequently, two samples from each constellation (316L at the bottom layers and 17–4PH at the top layers as well as 17–4PH at the bottom and 316L to the top) were sintered at four different maximum temperatures for two hours (see Fig. 3).

To quantify the shrinkage, a Digital Vernier caliper was used to measure the dimensions of the cubes in X, Y, and Z. The shrinkage was calculated as stated in the Eq. (1).

$$\text{Percent of shrinkage} = \frac{l_o - l_i}{l_o} \times 100\% \quad (1)$$

Where l_o is the length of interest in the green part and l_i is the length

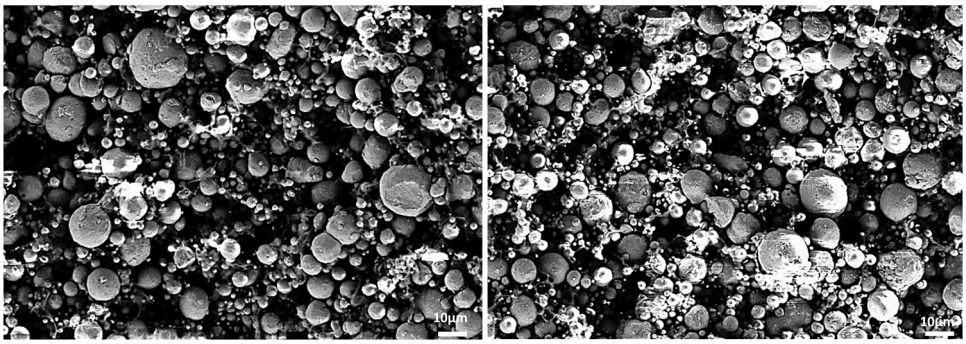

Fig. 1. SEM images of debinded PT+A GmbH 316L filament (left) and 17–4PH filament (right).

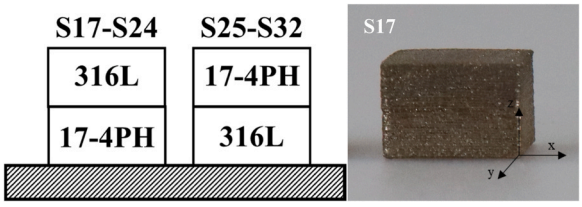

Fig. 2. Representation of selected test cubes after sintering manufactured with different sintering profiles.

Table 2
Sintering temperatures and deposition orders for the samples labeled S1 to S32.

Ref.	Sintering T. (°C)	Deposition order (Top/Bottom)
S1, S2	1286	316L
S3, S4	1310	316L
S5, S6	1320	316L
S7, S8	1330	316L
S9, S10	1286	17-4PH
S11, S12	1310	17-4PH
S13, S14	1320	17-4PH
S15, S16	1330	17-4PH
S17, S18	1286	316L/17-4PH
S19, S20	1310	316L/17-4PH
S21,S22	1320	316L/17-4PH
S23,S24	1330	316L/17-4PH
S25,S26	1286	17-4PH/316L
S27,S28	1310	17-4PH/316L
S29,S30	1320	17-4PH/316L
S31,S32	1330	17-4PH/316L

Table 3
Printing parameters for manufacturing MM stainless steel green parts using a Renkforce RF 2000 3D printer.

Extrusion temperature (°C)	140
Heat bed temperature (°C)	60
Printing speed (mm/min)	2100
Extrusion multiplier	1.35
Skirt layer	3
Retraction distance (mm)	4.5
Layer height (mm)	0.2
Infill (%)	100
Filament Diameter (mm)	2.85
Nozzle Diameter (mm)	0.4

of interest after sintering. The Measurements were conducted twice, both at the edges and in the center of the specimen. Following Buehler guidelines, samples were, embedded, and then ground and polished with progressive sanding papers and polishing solutions indicated for Fe-based alloys using a Vector Power Head (Buehler GmbH, Düsseldorf, Germany). Optical microscopy examinations were carried out using a

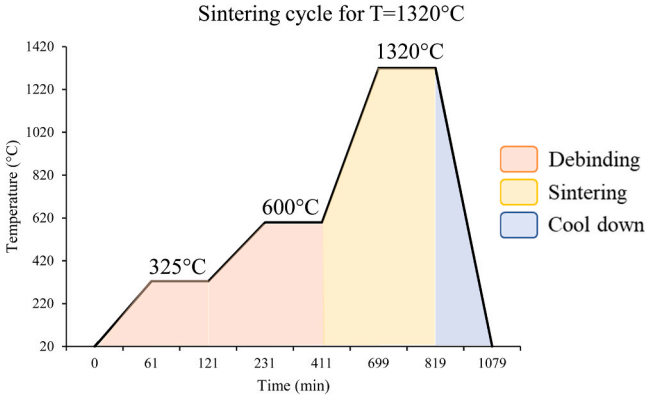

Fig. 3. Representation of the sintering cycle performed at 1320 °C.

MBL 3300 microscope (A.KRÜSS Optronic GmbH, Hamburg, Germany) to obtain further information about the internal structure of the material. Cross-section images of the samples were taken and treated using the image processing software ImageJ to determine density. The images were changed to 8-bit type and adjusted through threshold until the different microstructures were eliminated and only very small to big pores were visible. This methodology guaranteed to obtain a contrast image that includes all the areas occupied by the pores including little to null regions from grain borders. The bulk density of each region was determined through area measurement of each side of the constellation. Before deeper microscopy analysis, the samples were etched to Fry's (5 g CuCl 2, 40 mL HCl, 30 mL H_2O, and 25 mL ethanol) chemical reagent was applied for 15 s. Scanning Electron Microscopy (SEM) using a Zeiss Supra 55 VP FEG-SEM with Variable Pressure Mode (Carl Zeiss AG, Jena, Germany) was used to study the surface structure in the interface of the materials in more detail. Energy-dispersive X-ray spectroscopy (EDS) analysis was performed to investigate the chemical composition of the materials in the interface region.

3. Results and discussion

3.1. Shrinkage

The specimens tested in each constellation didn't show any significant deformation of the components as it was observed in the reference [38]. This indicates that the fabrication method and the co-sintering were successful. Fig. 4 displays the measured shrinkage in each space direction as a function of the sintering temperature.

The shrinkage in 316L specimens is very coherent in both X and Y showing a similar pattern that reaches its peak at 1310 °C with 15.88% and 16.22% in X and Y respectively. The shrinkage drops at 1320 °C to 11.76% in X and 12.09% in Y to rise again to more distinct to 12.80% and 13.94% at 1330 °C. The shrinkage experimented in the Z axis seems

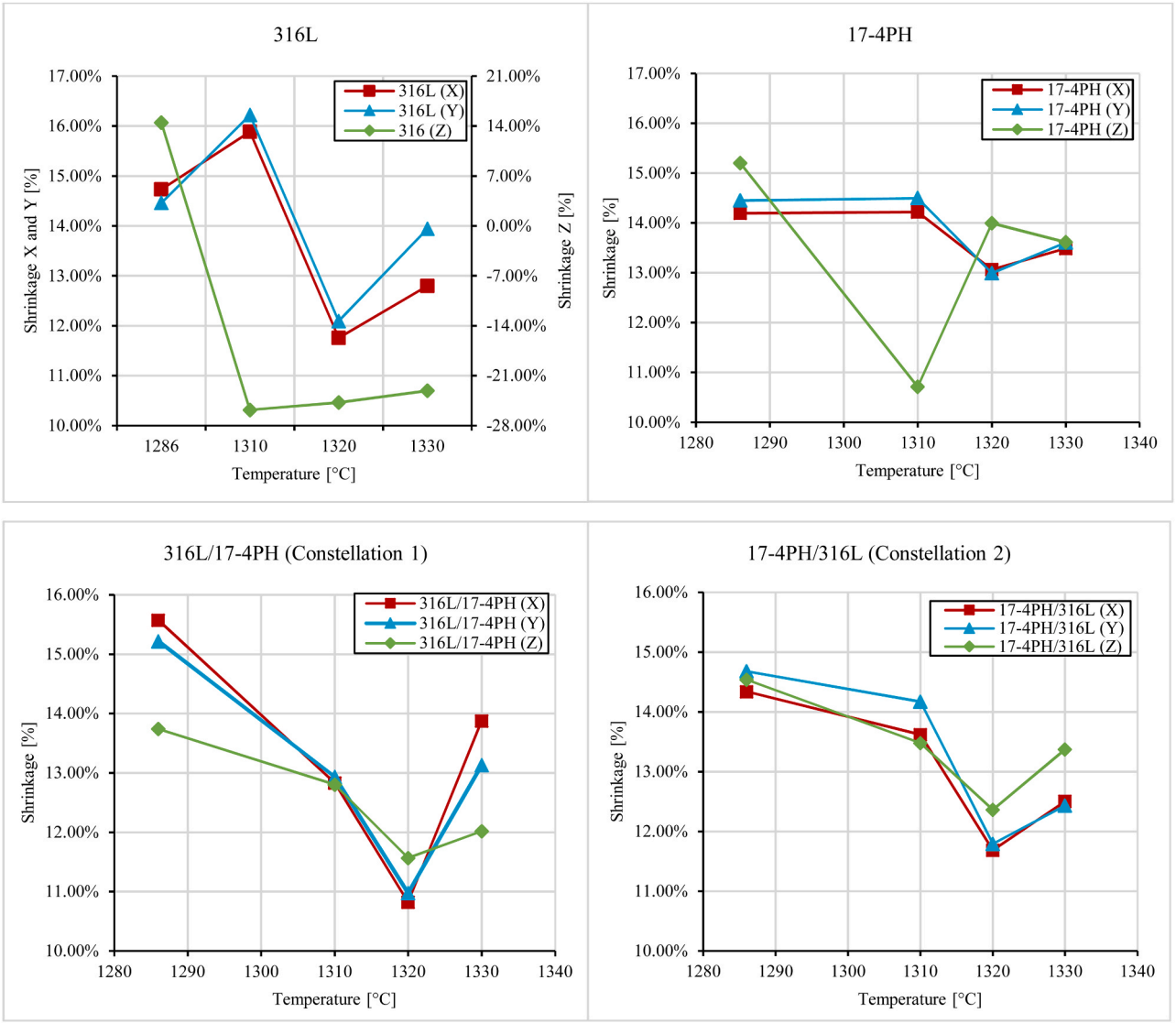

Fig. 4. Shrinkage evolution over temperature for a) 316L, b) 17–4PH, c) 316L/17–4PH and d) 17–4PH/316L samples.

to not follow the trend as the samples tend to grow in the Z axis (Fig. 4 top left, right axis). This effect manifested itself in the samples as a swelling (negative shrinkage) in the Z-axis and only occurred in the 316L samples at 1310 °C (−27%), decreasing at 1320 °C (−25%) and 1330 °C (−22%) respectively. The rounded top and bottom surface suggest that the sample displaced the material as a result of extreme swelling in X and Y. These samples' density was very low which might indicate that the part was not as dense as expected leading to the filling of this gaps during sintering and a lose of geometrical proportions in the Z axis as it was also observed in the reference [37].

17–4PH samples experimented a similar trend to the 316L samples existing with just a 1.77%, 1.91%, 0.54%, and 0.89% difference between X and Y at 1286 °C, 1310 °C, 1320 °C and 1330 °C respectively. The shrinkage in Z experiments showed an abrupt change at 1310 °C had a lower value of 10.71%, followed by a rise to 14% at 1320 °C and maintained at 13.61% at 1330 °C.

The Multimaterial samples follow a mirrored trend to the 17–4PH behavior in X and Y, having the lowest shrinkage value at 1320 °C of 10.98% and 11.79% for 316L/17–4PH and 17–4PH/316L respectively. Both constellations raise their shrinkage to 13.87% and 12.50% in X and 13.13% and 12.43% in Y for 316 L/17–4PH and 17–4PH/316L respectively. The behavior in the Y dimension shows a much similar trend to the one in X and Y contrary to the single material samples. The positioning of the material appears to play a negligible role when compared to the influence of the sintering temperature. The values obtained by the MM samples are the lowest in the graphs suggesting that the MM are less affected by the shrinkage tendency. The values obtained for the 17–4PH/316L sample are slightly higher than their counterpart. One hypothesis on this could be that the material standing on top of the sample might be receiving more heat than the one below which could make sense since 17–4PH has a lower melting point than 316L. A prolonged exposure time to heat might have resulted in increased deformation, however, the 17–4PH CTE is lower than 316L CTE.

Overall, coherent values between X and Y deformation are found in single material printing, while Multimaterial samples show slight variation. More interestingly, MM samples experiment with different shrinkage values for the two constellations proposed. This slight difference could be associated with a particle compensation of the shrinkage behavior as both materials deform in different amount. Interestingly, all values obtained for 1310 °C, 1320 °C, and 1330 °C in both constellations are lower than any of their single material counterparts, which means that an average CTE is not ruling the samples, but one that is actually closer to 17–4Ph or lower is. Nevertheless, the values only find proportion agreement at 1300 °C, therefore a more intensive dimensional study should be carried out.

3.2. Optical density measurement

The optical density measurements of the samples were within the expected range of conventional 316L and 17–4PH parts. The density was measured using SEM images and calculated from the number of pores. Optical measurements a predominantly used for process monitoring applications and allow an exact observation of specific criterias and indicators [39]. In contrast to Archimedes' principle, the current measurement method offers a more nuanced approach by taking into account the specific section under consideration. However, it is essential to acknowledge that Archimedes' principle comes with certain significant drawbacks. One notable limitation is its tendency to measure open porosities as dense, thereby potentially distorting the overall value. This flaw becomes particularly pronounced when dealing with multimaterial components, as the method is unable to measure the density of individual materials separately. This allows for a more precise characterization, circumventing the limitations associated with Archimedes' principle, especially in scenarios involving complex material compositions and transitions.In the section shown in Fig. 5, the calculated density for 316L is 97.4% and for 17–4PH 97.6%. These measurements need a secondary and morecomprehensive image based characterization method as these values correspond to some specific regions and the density of MEX/M samples could vary dramatically along the print direction due to printing and/or extrusion voids [40].

The samples show small signs of printing voids at the interface between the two materials, showing good deposition between one material onto the other. Besides those, the samples show good bonding and a small warpage indicating that the fabrication method was successful, and the materials were of high density reaching MIM standard according to ISO 22068:2012.

3.3. Microstructure

Optical microscopy (OM) was performed on the not-etched and etched specimens. No cracks nor wrecks are visible indicating no severe thermal stresses were generated during the solidification. Only in the case of 17–4PH as the top layers and 316L as the bottom layers, as in Fig. 6(a), are isolated larger pores visible at the sintering temperature of 1310 °C in the zone of material change. Likewise, a more defined grain boundary can be appreciated at 1310 °C. This region, which initially indicated the limit between the two materials shows the increased formation of expected carbides and σ-phase as a result of diffusion. The bigger pores found in this region may have originated during the printing step as the deposition of one material onto the other could lead to voids or gaps generated during the printing. A less probable justification for the large pores close to the interface at higher sintering temperatures could be due to increased stress between the materials due to thermal expansion and sintering shrinkage mismatch, however no cracks are visible. It can be assumed that in this case the diffusion process at higher temperatures as a driving force was amplified has caused more precipitations at the interface. On the contrary, these observations are not as evident as in the other material constellations at the material transition (e.g. Fig. 6(b)).

For 17–4PH the characteristic martensitic matrix with small δ-ferrite islands at the grain boundary can be identified. The 316L side shows an austenitic matrix with δ-ferrite in the grain borders. Both sides show in-grain precipitation of carbides. More pores are observed in the 316L layers than in the 17–4PH layers regardless of the sintered temperature, which is interesting as the martensitic alloy has a lower sintering temperature than the austenitic alloy. A typical grain growth at higher sintering temperatures can be observed in both stainless-steel alloys.

Fig. 7 shows the interfaces of the different constellations at two sintering temperatures and etching times. It is clear that no larger pores occur in the material transition independent of the sintering temperature, confirming that larger pores at the interface might have originated as printing voids. Furthermore, it can be observed that components of 17–4PH have diffused into the austenitic phase of 316L so that there is no clear boundary between the layers. The diffusion path achieved at 1310 °C is greater than at 1286 °C by about 50 micrometers (also compare Fig. 6). The constellation does not affect this.

3.4. SEM and EDS Analysis

As can be appreciated in Fig. 8, the material transition for S24 is inconspicuous. Ni concentration is higher in the 316L region at 6.59 wt % than in the 17–4PH area at 5.03 wt%. According to [35], the concentration difference shows that Ni from the 316 L region diffused towards the 17–4PH region as expected. In addition, the copper content is 2.92 wt% in the 316L and 5.03 wt% in the 17–4PH region, leading to two assumptions: the location of the Cu in the 316L region attends to no other explanation but the etchant containing CuCl, copper oxide may have formed on the surface during SEM preparation, or Cu diffused deep into the 316 region. The second assumption is more likely true since molybdenum was detected at 1.57 wt% in the 316L area and 1.44 wt% in the 17–4PH region. Besides the Cu contamination from etching, a significant diffusion between both materials can be denoted for the rest of the alloying elements (Mo, Ni, Cr). Also visible in this image are increased pores in the region of 316L.

4. Conclusion and outlook

With regards to MM components, MEX/M technology provides an advantageous platform to produce said components, without any major adaptations to existing equipment. Unlike the MIM process, the MEX/M process does not require a powder layering technique or co-injection molding process [30], making functional prototypes easy and cost-effective to manufacture. The main conclusions are:

- Within this work, it was shown that MM steel cubes made of 316L and 17-4PH in two different constellations were manufactured using commercial equipment and filament feedstock. The samples S7 and S8 at a sintering temperature of 1330 °C showed the best results with

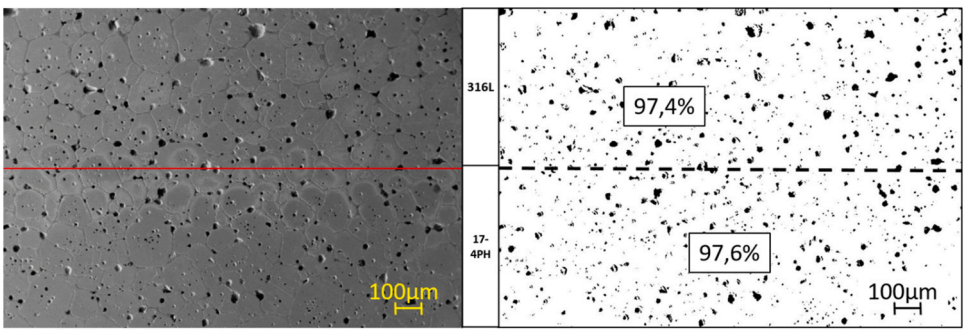

Fig. 5. SEM image of S24 (316 L/17–4PH sintered at 1330 °C) (left), and calculated density using ImageJ software (right).

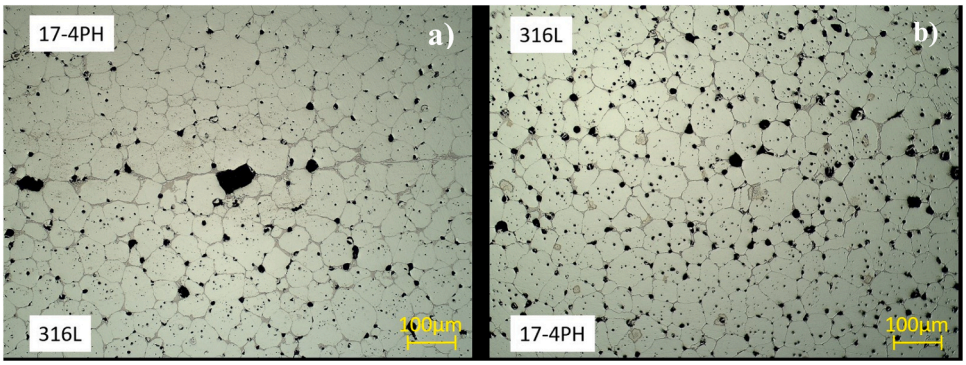

Fig. 6. Optical microscopy image of a) S27 (17–4PH/316 L sintered at 1310 °C); and b) S17 (316 L/17–4PH sintered at 1286 °C).

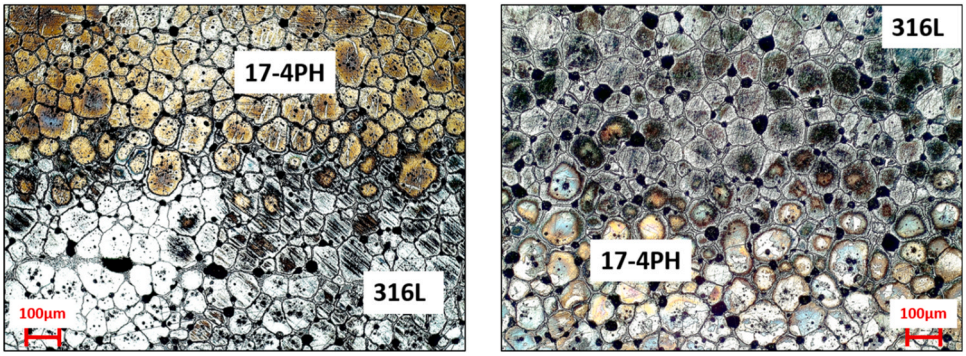

Fig. 7. Optical microscopy of the etched specimens a) S28 (17–4PH/316L sintered at 1310 °C) and etchingtime 15 s, and b) S18 (316 L/17–4PH sintered at 1286 °C) and etching time 20 s.

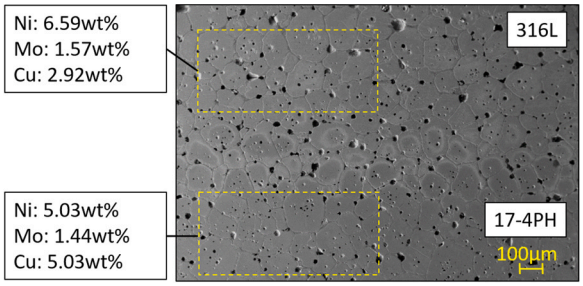

Fig. 8. SEM image of S24 (316L/17–4PH sintered at 1330 °C) and the EDS wt% measurements of Cu, Ni, and Mo at the areas highlighted.

average densities of 97.4% and 97.6%, respectively. The findings also confirm that the sintering temperature, rather than the deposition order of the materials, appears to be the key factor controlling the shrinkage of these samples. However, the shrinkage behaviour was slightly different for both constellations reaching a maximum difference of 1.44% in Z axis for 1300 °C. The difference between the values obtained for single-material and MM printing might be caused by the disposition of the samples in the furnace or due to CTEs mismatch, leading to partial compensation between them. Further in-deep investigations on this matter are needed to support the hypothesis.

- The calculated density from the image analysis also showed that the MIM standard according to ISO 22068:2012 could be met. However, a more comprehensive optical density measurement such as layer by layer x-ray image analysis must be carried out, so that an overall statement about the density of the investigated samples can be made. Further in-depth study of the density will also be covered to explore the influence of printing voids from the extrusion process into the sintered samples, exploring also the horizontal cross-section of both regions.
- As opposed to other works [27], the parts produced showed no major deformation, wherein functional parts without the need for post-processing seem to be a possible task. The measured shrinkage in each coordinate direction was consistently smaller than what might have been expected based on the individual properties of 316L and 17-4PH stainless steels. Although precise expected values were not available, the results obtained cannot provide a rigorous quantitative statement about this observation. Therefore, a statistical study such as ANOVA should be carried out in the future. Further analysis of the shrinkage can be done on complex geometries such as cylindrical structures, overhangs, walls, different infill patterns, etc. Additionally, a machine learning-based methodic approach can be conducted to identify the optimal infill pattern as in to avoid anisotropic shrinkage behaviour.

In the future, the interdiffusion of alloying elements as well as the generation of undesired intermetallic compounds for both materials at the interface need to be covered in deep. Aiming to improve the bonding of the MM samples, the mechanical properties need to be studied as well. Additionally, it is necessary to explore various multimaterial design features to establish design guidelines for the successful manufacturing of multimaterial components such as in the case of single materials [41, 42]. The results obtained in the forthcoming studies will reveal how the parameters involved in all the stages of the chain value (extrusion, debinding, and sintering) affect the mechanical strength at the interface, and therefore, shed light on their limitations for applications. In the future, different types of infill structures have to be investigated to achieve the desired mechanical properties depending on the constellations [43]. This combination of materials can potentially be used for application areas where magnetic and non-magnetic regions are required in a component such as sensors and actuators for automotive or

aerospace applications. Ultimately, topology-optimized multimaterial components can also be additively manufactured [44], allowing locally advantageous material properties to be incorporated into a single unit.

CRediT authorship contribution statement

Karim Asami: Conceptualization, Data curation, Formal analysis, Investigation, Methodology Writing – original draft, Writing – review & editing. **José M. Crego Lozares:** Data curation, Formal analysis, Investigation, Validation, Visualization, Methodology, Writing – review & editing. **Abid Ullah:** Data curation, Formal analysis, Investigation, Validation, Visualization, Methodology, Writing – review & editing. **Bastian Bossen:** Resources, Validation, Visualization, Writing – review & editing. **Leighton Clague:** Resources, Validation, Visualization, Methodology, Writing – original draft, Writing – review & editing. **Claus Emmelmann:** Resources, Validation, Visualization, Project administration, Supervision.

Declaration of Competing Interest

The authors declare that they have no known competing financial interests or personal relationships that could have appeared to influence the work reported in this paper.

Data Availability

Data will be made available on request.

Acknowledgments

The authors would like to acknowledge the support and affiliation with the Hamburg University of Technology (TUHH). The authors would also like to acknowledge the support from the REDI Program, a project that has received funding from the European Union's Horizon 2020 research and innovation program under the Marie Skłodowska-Curie grant agreement no. 101034328.This paper reflects only the author's view and the Research Executive Agency is not responsible for any use that may be made of the information it contains.

Author Agreement Statement and Contributions

We the undersigned declare that this manuscript is original, has not been published before, and is not currently being considered for publication elsewhere.

We confirm that the manuscript has been read and approved by all named authors and that there are no other persons who satisfied the criteria for authorship but are not listed. We further confirm that the order of authors listed in the manuscript has been approved by all of us.

We understand that the Corresponding Author is the sole contact for the Editorial process. He/she is responsible for communicating with the other authors about progress, submissions of revisions, and final approval of proofs.

References

[1] M. Khorasani, A. Ghasemi, B. Rolfe, I. Gibson, Additive manufacturing a powerful tool for the aerospace industry, Rapid Prototyp. J. 28 (2022) 87–100.
[2] A. Ur Rehman, A. Ullah, T. Liu, R. Ur Rehman, M.U. Salamci, Additive manufacturing of Al2O3 ceramics with MgO/SiC contents by laser powder bed fusion process, Front. Chem. 11 (2023) 1034473.
[3] O.A. Mohamed, S.H. Masood, J.L. Bhowmik, Experimental investigations of process parameters influence on rheological behavior and dynamic mechanical properties of FDM manufactured parts, Mater. Manuf. Process. 31 (2016) 1983–1994.
[4] C.S. Lee, S.G. Kim, H.J. Kim, S.H. Ahn, Measurement of anisotropic compressive strength of rapid prototyping parts, J. Mater. Process. Technol. 187-188 (2007) 627–630.
[5] M. Sadaf, M. Bragaglia, F. Nanni, A simple route for additive manufacturing of 316L stainless steel via fused filament fabrication, J. Manuf. Process. 67 (2021) 141–150.
[6] C. Tosto, J. Tirillò, F. Sarasini, G. Cicala, Hybrid metal/polymer filaments for fused filament fabrication (FFF) to print metal parts, Appl. Sci. 11 (2021) 1444.
[7] Y. Thompson, J. Gonzalez-Gutierrez, C. Kukla, P. Felfer, Fused filament fabrication, debinding and sintering as a low cost additive manufacturing method of 316L stainless steel, Addit. Manuf. 30 (2019), 100861.
[8] D. Jiang, F. Ning, Additive manufacturing of 316L stainless steel by a printing-debinding-sintering method: effects of microstructure on fatigue property, J. Manuf. Sci. Eng. 143 (2021).
[9] D.F. Heaney, Handbook of metal injection molding, Woodhead Publishing.
[10] C. Suwanpreecha, A. Manonukul, A review on material extrusion additive manufacturing of metal and how it compares with metal injection moulding, Metals 12 (2022) 429.
[11] S. Jadhav, M.S. Bajestani, S. Islam, M.A. Karim, C.J. Kim, H.-J. Lee, Y.T. Cho, et al., Materials characterization of Ti6Al4V to NbZr1 bimetallic structure fabricated by wire arc additive manufacturing, Mater. Today Commun. (2023), 106934.
[12] Y. Thompson, K. Zissel, A. Förner, J. Gonzalez-Gutierrez, C. Kukla, S. Neumeier, P. Felfer, Metal fused filament fabrication of the nickel-base superalloy IN 718, J. Mater. Sci. 57 (2022) 9541–9555.
[13] J. Abel, U. Scheithauer, T. Janics, S. Hampel, S. Cano, A. Müller-Köhn, A. Günther, et al., Fused filament fabrication (FFF) of metal-ceramic components, J. Vis. Exp. JoVE (2019).
[14] J. Wang, Some critical issues for injection molding, BoD–Books on Demand, 2012.
[15] J. Gonzalez-Gutierrez, S. Cano, S. Schuschnigg, C. Kukla, J. Sapkota, C. Holzer, Additive manufacturing of metallic and ceramic components by the material extrusion of highly-filled polymers: a review and future perspectives, Mater. (Basel, Switz.) 11 (2018).
[16] P. Imgrund, A. Rota, M. Wiegmann, Powder Injection Moulding Micro MIM: Investigation of Material Interfaces Obtained by Two-Component-Micro-MIM and Co-Sintering.
[17] V. Piotter, E. Honza, A. Klein, T. Mueller, K. Plewa, Powder injection moulding of multi-material devices, Powder Metall. 58 (2015) 344–348.
[18] G.B. Dutra, M. Mulser, R. Calixto, F. Petzoldt, Investigation of material combinations processed via two-component metal injection moulding (2C-MIM), MSF 727-728 (2012) 248–253.
[19] P. Imgrund, A. Rota, F. Petzoldt, A. Simchi, Manufacturing of multi-functional micro parts by two-component metal injection moulding, Int J. Adv. Manuf. Technol. 33 (2007) 176–186.
[20] C. Pascal, J.-M. Chaix, F. Doré, C.H. Allibert, Design of multimaterial processed by powder metallurgy: processing of a (steel/cemented carbides) bilayer material, J. Mater. Process. Technol. 209 (2009) 1254–1261.
[21] J. Cheng, L. Wan, Y. Cai, J. Zhu, P. Song, J. Dong, Fabrication of W–20wt%Cu alloys by powder injection molding, J. Mater. Process. Technol. 210 (2010) 137–142.
[22] M. Mulser, T. Hartwig, F. Petzoldt, Tungsten-copper/stainless steel Bi-material parts by 2C-MIM (2012).
[23] T. Mueller, V. Piotter, K. Plewa, J. Prokop, H.J. Ritzhaupt-Kleissl, J. Hausselt, Complex shaped micro components produced by powder injection molding, in: Proceedings of 5th 4 M Conference, pp. 429–432.
[24] T. Moritz, Two-component CIM parts for the automotive and railway sectors, Powder Inject. Mould. Int. 2 (2008) 38–39.
[25] A. Ruh, V. Piotter, K. Plewa, H.-J. Ritzhaupt-Kleissl, J. Hausselt, Development of two-component micropowder injection molding (2C-MicroPIM)-process development, Int. J. Appl. Ceram. Technol. 8 (2011) 610–616.
[26] A. García-Collado, J.M. Blanco, M.K. Gupta, R. Dorado-Vicente, Advances in polymers based multi-material additive-manufacturing techniques: state-of-art review on properties and applications, Addit. Manuf. 50 (2022), 102577.
[27] B. Tomar, S. Shiva, T. Nath, A review on wire arc additive manufacturing: processing parameters, defects, quality improvement and recent advances, Mater. Today Commun. 31 (2022), 103739.
[28] R. Freund, H. Watschke, J. Heubach, T. Vietor, Determination of influencing factors on interface strength of additively manufactured multi-material parts by material extrusion, Appl. Sci. 9 (2019) 1782.
[29] S. Hasanov, A. Gupta, A. Nasirov, I. Fidan, Mechanical characterization of functionally graded materials produced by the fused filament fabrication process, J. Manuf. Process. 58 (2020) 923–935.
[30] H. Watschke, L. Waalkes, C. Schumacher, T. Vietor, Development of novel test specimens for characterization of multi-material parts manufactured by material extrusion, Appl. Sci. 8 (2018) 1220.
[31] J. Yin, C. Lu, J. Fu, Y. Huang, Y. Zheng, Interfacial bonding during multi-material fused deposition modeling (FDM) process due to inter-molecular diffusion, Mater. Des. 150 (2018) 104–112.
[32] T. Rosnitschek, A. Seefeldt, B. Alber-Laukant, T. Neumeyer, V. Altstädt, S. Tremmel, Correlations of geometry and infill degree of extrusion additively manufactured 316L stainless steel components, Mater. (Basel, Switz.) 14 (2021).
[33] M. Mousapour, M. Salmi, L. Klemettinen, J. Partanen, Feasibility study of producing multi-metal parts by fused filament fabrication (FFF) technique, J. Manuf. Process. 67 (2021) 438–446.
[34] J. Abel, U. Scheithauer, T. Janics, S. Hampel, S. Cano, A. Müller-Köhn, A. Günther, et al., Fused filament fabrication (FFF) of metal-ceramic components, JoVE (J. Vis. Exp.) (2019), e57693.
[35] A. Simchi, A. Rota, P. Imgrund, An investigation on the sintering behavior of 316L and 17-4PH stainless steel powders for graded composites, Mater. Sci. Eng.: A 424 (2006) 282–289.
[36] V. Martin, J.-F. Witz, F. Gillon, D. Najjar, P. Quaegebeur, A. Benabou, M. Hecquet, et al., Low cost 3D printing of metals using filled polymer pellets, HardwareX 11 (2022), e00292.

[37] S. You, D. Jiang, F. Wang, F. Ning, Anisotropic sintering shrinkage behavior of stainless steel fabricated by extrusion-based metal additive manufacturing, J. Manuf. Process. 101 (2023) 1508–1520.
[38] B. Tomar, S. Shiva, T. Nath, A review on wire arc additive manufacturing: processing parameters, defects, quality improvement and recent advances, Materials Today, Communications 31 (2022), 103739.
[39] K. Rane, K. Castelli, M. Strano, Rapid surface quality assessment of green 3D printed metal-binder parts, J. Manuf. Process. 38 (2019) 290–297.
[40] G. Singh, J.-M. Missiaen, D. Bouvard, J.-M. Chaix, Copper additive manufacturing using MIM feedstock: adjustment of printing, debinding, and sintering parameters for processing dense and defectless parts, Int J. Adv. Manuf. Technol. 115 (2021) 449–462.
[41] D. Herzog, K. Asami, C. Scholl, C. Ohle, C. Emmelmann, A. Sharma, N. Markovic, et al., Design guidelines for laser powder bed fusion in Inconel 718, J. Laser Appl. 34 (2022).
[42] Design Guidelines For Green Parts Manufactured With Stainless Steel In The Filament Based Material Extrusion Process For Metals (MEX/M), World PM 2022 Congress Proceedings, 2022.
[43] K. Asami, S. Roth, M. Krukenberg, T. Röver, D. Herzog, C. Emmelmann, Predictive modeling of lattice structure design for 316L stainless steel using machine learning in the L-PBF process, J. Laser Appl. 35 (2023).
[44] T. Röver, M. Bader, K. Asami, C. Emmelmann, I. Kelbassa, Development and assessment of a methodology for abstraction of topology optimization results to enable the substitution of optimized beams, J. Laser Appl. 35 (2023).